Bond behaviour of ribbed near-surface-mounted iron-based shape memory alloy bars with short bond lengths

Author(s):
Schranz, Bernhard; Czaderski, Christoph; Vogel, Thomas; Shahverdi, Moslem

Publication date:
2020-06

Permanent link:
https://doi.org/10.3929/ethz-b-000414700

Originally published in:
Materials & Design 191, https://doi.org/10.1016/j.matdes.2020.108647

Materials and Design 191 (2020) 108647

Contents lists available at ScienceDirect

Materials and Design

journal homepage: www.elsevier.com/locate/matdes

Bond behaviour of ribbed near-surface-mounted iron-based shape memory alloy bars with short bond lengths

Bernhard Schranz [a,b], Christoph Czaderski [a], Thomas Vogel [b,c], Moslem Shahverdi [a,d,*]

[a] Swiss Federal Laboratories for Materials Science and Technology (Empa), Dübendorf, Switzerland
[b] Department of Civil, Environmental and Geomatic Engineering (D-BAUG), ETH, Zürich, Switzerland
[c] Institute of Structural Engineering (IBK), ETH, Zürich, Switzerland
[d] School of Civil Engineering, University of Tehran, Tehran, Iran

HIGHLIGHTS

- Three pull-out failure modes were revealed: splitting, combined splitting and pull-out, splitting of the cube.
- The failure modes mainly depend on cover depth, mortar and concrete strength, and bar diameter.
- Longitudinal splitting cracks were observed with an image correlation system during experiments with low cover depth.
- Stainless steel bars showed lower bond strength than memory-steel bars with non-linear stress-strain behaviour.
- Analytical modelling reproduced bond stress, bar strain, and slip, as well as load capacity of the bonded joint.

GRAPHICAL ABSTRACT

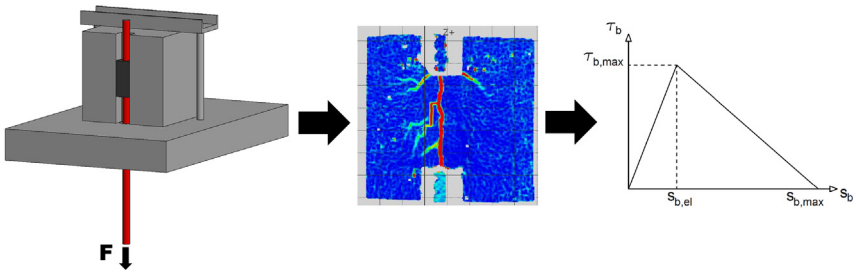

ARTICLE INFO

Article history:
Received 5 November 2019
Received in revised form 10 March 2020
Accepted 13 March 2020
Available online 14 March 2020

Keywords:
Iron-based
Shape memory alloy
Near-surface-mounted
Strengthening
Concrete structures

ABSTRACT

Many existing concrete buildings worldwide require improvement in structural integrity. Previous research has proven the effectiveness of iron-based shape memory alloy (Fe-SMA or memory-steel) reinforcements for the prestressed strengthening of structures. The unique function of the material, i.e., the so-called shape memory effect, enables cost-effectiveness and presents simple ways to prestress defective building components. Ribbed memory-steel bars have only been available recently. This study aimed to investigate their performance in a novel strengthening technique, named near-surface mounted (NSM) method. Bond experiments with short bond lengths were performed to investigate the feasibility of this configuration and to identify the effects of several design parameters including: groove dimensions, bar diameter, bar material, cover depth, mortar strength, and concrete strength. The use of a digital image correlation system enabled detailed measurements of slips, crack width, and surface strain.

An analytical procedure based on the differential equation of bond behaviour was developed, which enabled the calculation of slip, strain, bond shear stress, and load capacity. The results show that ribbed memory-steel bars can be used in an NSM configuration due to high bond capacity. The cover depth, substrate strength and elastic modulus had a significant effect on the failure mode and bond capacity.

Abbreviations: BSL, bond shear stress–slip law; CFRP, carbon-fibre reinforced polymer; DIC, digital image correlation; Fe-SMA, iron-based shape memory alloy; FRP, fibre-reinforced polymer; LVDT, linear variable differential transformer (displacement sensor); NSM, near-surface mounted; RC, reinforced concrete.

* Corresponding author at: Empa, Department 303, Überlandstrasse 129, 8600 Dübendorf, Switzerland.
E-mail addresses: moslem.shahverdi@empa.ch, moslem.shahverdi@ut.ac.ir (M. Shahverdi).

https://doi.org/10.1016/j.matdes.2020.108647

Notation

A_s	bar area
A_c	concrete area
c	cover depth
c_{max}	cover towards side edge
c_{min}	cover towards bottom edge
d_b	bar diameter
d_{bar}	displacement bar
$d_{concrete}$	displacement concrete
d_g	groove depth
ε_{bI}	strain in Zone I
ε_{bII}	strain in Zone II
ε_u	failure strain
E_s	elastic modulus of bar
E_c	elastic modulus of concrete
F_{br}	calculated pull-out load
$F_{max,test}$	maximum tested load capacity
F_{max}	maximum load
f_{cm}	mean concrete strength
f_{tm}	mean tensile strength
f_{cc}	concrete compressive strength
f_{mc}	mortar compressive strength
l_b	bond length
$R_{p0.2}$	0.2% proof stress
R_m	tensile strength
$\sigma_{max,bar}$	maximum axial stress of bar
s_b	bar slip
s_{bI}	slip in Zone I
s_{bII}	slip in Zone II
$s_{b,el}$	elastic slip
$s_{b,max}$	maximum slip
$s_{fr,Fmax}$	free-end slip at maximum load
$s_{ls,Fmax}$	loaded-end slip at peak load
$\tau_{b,max}$	maximum bond shear stress
$\tau_{bmax,fib}$	maximum calculated bond shear stress acc. to fib
$\tau_{max,test}$	maximum tested bond shear stress
$\tau_{bu,split}$	maximum calculated bond shear stress at splitting failure
w_c	crack width
w_g	groove width
x	length coordinate along bar
x_0	length coordinate, where Zone I and Zone II are separated

1. Introduction

1.1. Strengthening of concrete structures

Existing concrete structures are receiving increasing attention from researchers due to current issues of sustainability and efficiency in the building industry. Several studies now focus on the strengthening of defective concrete structures. State-of-the-art strengthening procedures include the replacement of corroded reinforcement and concrete, as well as installation of carbon-fibre reinforced polymer (CFRP) elements [1]. Also the application of textile reinforced mortar (TRM) has shown potential for the structural enhancement of concrete buildings [2,3].

Non-prestressed measures are usually sufficient if only the ultimate limit state performance of a structure needs to be improved. In contrast, prestressing methods are more effective when deformations and crack widths must be reduced based on the serviceability limit-state design requirements. Prestressing measures are usually costly and time-consuming. CFRP strips are commonly used for prestressing existing structures [4,5]. However, the number of site applications using prestressed CFRP strips in is limited owing to their high costs.

1.2. Iron-based shape memory alloy (memory-steel) as a strengthening material

The use of iron-based shape memory alloys (Fe-SMA or memory-steel) for prestressing reinforced concrete (RC) structures started several years ago [6–8]. The term, 'shape memory alloy', describes the unique property of this material to transform its crystal structure after initial deformation when subjected to heat [9]. During the initial deformation, some parts of the Austenitic lattice structure transform to Martensite. If the material is then heated, the Martensitic structures transform back to Austenite, leading to a contraction of the Fe-SMA element, and hence, the reversal of a part of the initial deformation [9]. If the contraction is hindered by mechanical fixation, stress known as 'recovery stress' is built up in the material [10]. The recovery stress can be used for the prestressing of building components such as beams and slabs. This prestressing technique does therefore not rely on hydraulic jacks for prestressing. The prestressing process is hence simplified and accelerated greatly, furthermore, frictional losses do not occur in this method. In 2009, an Fe-17Mn-5Si-10Cr-4Ni-1(V,C) (mass%) Fe-SMA was developed [11] at the Swiss Federal Laboratories for Material Science and Technology (Empa). Strips and bars made from this alloy, which was later named memory-steel, exhibit high ductility, high tensile strength, higher corrosion resistance than conventional reinforcement bars, and, most importantly, the shape memory effect [12–14]. Since the development of the alloy, several investigations have proven the function of memory-steel strips and ribbed bars for structural strengthening. In [15], memory-steel strips were used to increase the cracking and yielding loads of concrete beams subjected to flexure. The authors of [16] successfully applied near-surface-mounted memory-steel strips for the flexural strengthening of concrete beams. The behaviour of strengthened beams was modelled in [17]. In [18], prototype memory-steel bars were utilised in an additional shotcrete layer to effectively increase the cracking load, yielding load of the internal reinforcement, and load-carrying capacity. In [19], memory-steel elements were used to strengthen steel structures and connections. In the studies described above, the memory-steel components were either heated by electricity or infrared radiation. Since 2017, memory-steel reinforcements have already been used in several real-site applications. In [20], case studies of selected site applications were reported, proving the ease of application and effectiveness of memory-steel reinforcements. The current cost of strengthening applications using memory-steel can be seen as competitive to conventional techniques, considering the simple prestressing process and decreased effort in terms of fire protection. The involved costs are also assumed to decrease over time with economies of scale.

1.3. Near-surface-mounted strengthening

A novel strengthening method involves the installation of ribbed memory-steel bars in the concrete cover of existing structures. This method is known as the near-surface-mounted (NSM) application, where stainless steel or FRP bars and strips are commonly used [21]. In this method, grooves are first cut in the concrete cover using a diamond-saw and a chisel, followed by the installation of the elements using an adhesive. In the case of NSM, conventional prestressing procedures using hydraulic jacks are complex [22], require heavy mechanical anchorages, and are impractical in real applications. The authors of [6,16] successfully demonstrated the functionality of NSM memory-steel strips to increase the cracking, yielding, and ultimate load capacity of RC beams in flexure. In [23], NSM Fe-SMA smooth bars with mechanical end-anchorages were used in combination with epoxy resin to strengthen concrete beams. The results showed successful prestressing, the complexity of this kind of installation might be impractical for site

applications however. The use of ribbed memory-steel bars in contrast, enables simplification of the installation and prestressing process. The bars are mounted using a cementitious mortar, which simplifies the handling process and reduces the cost of bonding material, compared to epoxy resins.

The results of the current investigation contributed to the first real site applications of NSM memory-steel bars [24], as shown in Fig. 1. In both cases, concrete slabs were strengthened in the negative bending moment area.

1.4. Bond behaviour of near-surface-mounted bars

The bond behaviour of embedded steel bars has been investigated since 1900 [25]. Currently, the bond behaviour of an embedded ribbed bar is commonly characterized by its bond shear stress–slip behaviour. Bond behaviour can be determined using various types of bond tests, including standardised tests with short bond length such as the RILEM pull-out test [26] or a procedure by ASTM [27]. The bond length with small pull-out samples in experiments is usually limited to five times the bar diameter, which is assumed to represent the behaviour of an incremental bond element [28]. Modifications of tests with short bond length can be found in the literature, such as [29], where errors in the free-end slip measurements were avoided by placing a second unbonded area next to the end of the concrete specimen. The bond shear stress–slip law (BSL) obtained from pull-out tests is often used to solve the differential equation of bond behaviour [28], which enables the calculation of pull-out load capacity and effective bond length, as well as bond shear stress, slip, and strain curves along the bonded length [30]. Due to the fundamentally different bond behaviour of NSM memory-steel bars when compared to fully embedded steel bars, specific BSLs and their parameters must be determined in new experiments. A test setup for NSM fibre-reinforced polymer (FRP) bars was proposed in [31], where a C-shaped concrete element with a groove was used. In this setup, however, the complex geometry of the concrete element required casting of the groove, leading to the lower bond performance than when the groove had been cut with a diamond saw owing to smoothness of the groove surface. In [32], the bond behaviour of smooth sandblasted NiTi SMA bars was investigated in an NSM configuration, also using C-shaped concrete elements. The grooves in [32] were also prefabricated with the concrete element.

In [33], a minimum cover depth equalling the diameter of the embedded bar is suggested, to avoid premature bond failure and therefore lower bond stress due to splitting of the concrete cover. In an NSM strengthening configuration, these dimensions can often not be provided due to a limited existing concrete cover. Splitting has already been studied extensively, for example in [34–36], where it was found that this type of failure is more likely to occur when low-tensile strength concrete and low cover depth are used. The mechanism behind the splitting phenomenon is the stress transfer from axial pull-out load, to radial stresses in the surrounding material and consequently tangential tensile stresses in the cover, commonly referred to as the ring stresses [29,37].

Due to the absence of transverse confining reinforcement, splitting is also more likely to occur in NSM applications. The effect of the cover depth on bond strength has been studied in [34,36,38], with the result that the bond strength increases with increasing cover depth, the quantification varies throughout these investigations however. In [39], the experiments indicated an increase in bond strength of 0.18 MPa per millimetre cover depth, until it remains constant after a cover depth of four times the bar diameter.

Based on the findings of [21,29,40,41], the relevant failure modes in an NSM configuration are local failure of the filling material ('pull-out'), tensile cracking of the filling material ('splitting filling material'), tensile failure of the surrounding concrete ('splitting concrete'), or a combination. These studies reported that if cementitious mortar is used, the mortar cover is more likely to develop longitudinal splitting cracks due to lower tensile strength. The findings also showed that failure due to splitting of the surrounding concrete is more likely to occur if a ribbed bar is used since higher radial stresses lead to increased tensile cracks in the surrounding mortar.

1.5. Motivation

As explained from Sections 1.1 to 1.4, current strengthening methods are inefficient for improving the serviceability limit state performance of concrete structures. Previous research has already established the effectiveness of memory-steel reinforcement. Especially NSM methods have shown several advantages compared to external applications. Ribbed memory-steel bars show high potential to be used in an NSM configuration. Due to the novelty of the method, the effects of the different stress-strain behaviours of memory-steel bars compared to conventional steel bars, the installation under limited mortar cover, heating of the bar while being embedded, and the prestress before an external loading on the bond behaviour have not been studied so far to the best of the authors' knowledge.

1.6. Current investigation

In this study, the bond behaviour of near-surface-mounted memory-steel bars was studied experimentally using pull-out tests. The study focused on the effect of groove dimensions, bar diameter, cover depth, mortar strength, concrete strength, and bar material. An analytical model was developed, based on the differential equation of bond behaviour. The results of the developed model and existing design recommendations were compared with the test results.

(a) (b)

Fig. 1. First site applications of NSM memory-steel bars [24]. (a) Strengthening of a concrete cantilever slab, Münchenstein, Switzerland. (b) Strengthening of a concrete slab in the negative bending moment area, Winterthur, Switzerland.

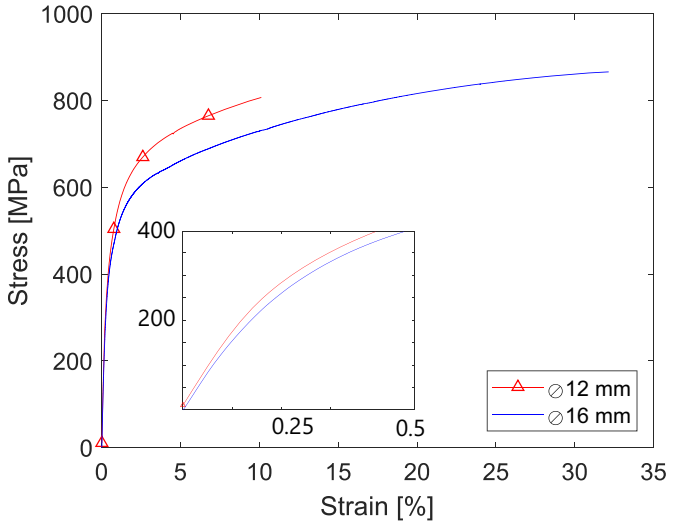

Fig. 2. Representative stress-stain behaviour of memory-steel bars with 12 mm diameter (red) and 16 mm diameter (blue).

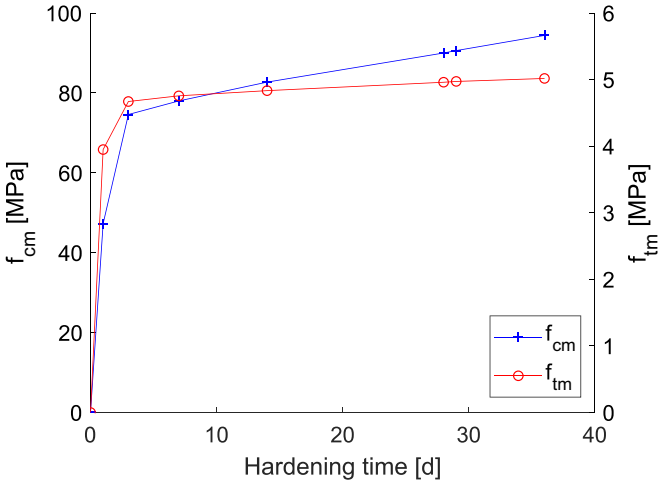

Fig. 3. Strength development of mortar.

2. Experiments

2.1. Materials

2.1.1. Iron-based shape memory alloy (memory-steel) bars

In this study, ribbed memory-steel bars with nominal bar diameters of 16 mm and 12 mm were used. The geometry of the ribs complied with British Standard 6744:2001 [42]. The bars were delivered by the Swiss company re-fer AG. The material has high tensile strength and ductility. The 12 mm diameter bars that were used in this investigation, however, were produced from an early prototype batch, resulting in lower tensile strength and failure strain. In Fig. 2, the stress-strain curves for the two bar diameters are compared. It is evident that between 500 MPa and 800 MPa, the slope of the 12 mm bar material was higher than that of 16 mm bars. This behaviour originates from a different mechanical straightening process after production (cold deformation), which seems to have a hardening effect on the 12 mm bars, and hence, leads to higher stiffness but less ductility. It should be noted that for the calculations of stress in the bar cross-section, a bar diameter of 11.5 mm was used instead of 12 mm. For the 16 mm bars, a diameter of 16 mm was used.

2.1.2. Stainless steel bars

For comparison, stainless steel bars [43] with a nominal diameter of 16 mm and the same geometry as the memory-steel bars were also used in the investigations. The bars were of type 1.4162 with a Young's modulus of 200 GPa, 0.2% proof stress $R_{p0.2}$ of 500 MPa, tensile strength R_m of 550 MPa, failure strain ε_u of 14%, and rib geometry according to British Standard 6744:2001 [42].

2.1.3. Concrete

Concrete cubes of 200 × 200 × 200 mm were used as the base members. Two different types of concrete were used. The concrete compression strength was determined by a compressive test, using 150 × 150 × 150 mm cubes. The concrete splitting tensile strength was determined by a splitting tensile test using 150 × 150 × 150 mm cubes. The first type (concrete number 1) had a 28-day compressive strength of 51.2 MPa and a splitting tensile strength of 4.0 MPa, whereas concrete number 2 had a 28-day compressive strength of 44.6 MPa and a splitting tensile strength of 3.7 MPa. For concrete number 2, a maximum 28-day compressive strength of 30 MPa was ordered. However, due to inaccuracies at the mixing plant, the received compressive strength was higher, and therefore, the difference in strength with concrete 1 was smaller. The compressive strength was determined with 150 × 150 × 150 mm concrete cubes. The strengths were determined on the same day as the pull-out experiments; the actual values are listed in Table 1.

2.1.4. Mortar

A cementitious mortar type SikaGrout-314 [44] was used as the bonding material. The material offers fast strength development with shrinkage compensation during hardening. The mixing was performed according to the recommendations of the manufacturer with a water/powder mix ratio of 0.10–0.11. The mix included aggregates with a maximum size of 4 mm. The strength development was investigated at different stages of hardening with 40 × 40 × 160 mm mortar prisms and 3 specimens per each batch. Fig. 3 depicts the strength development over time. The data indicates the properties of rapid hardening, with a

Table 1
Test matrix of the pull-out tests, Variables: d_g … groove depth, w_g … groove width, c … mortar cover, d_b … bar diameter, l_b … bond length, f_{cc} … compressive strength of concrete block at day of testing, f_{mc} … compressive strength of mortar at day of testing.

Group	Tests	d_g [mm]	w_g [mm]	c [mm]	d_b [mm]	Bar material	l_b [mm]	f_{cc} [MPa]	f_{mc} [MPa]
1	1–2	27	34	9	16	Fe-SMA	80	57	94 (36d)
2	3–4	51	34	33	16	Fe-SMA	80	57	94 (36d)
3	5–6	27	52	9	16	Fe-SMA	80	57	94 (36d)
4	7–9	27	34	9	16	Fe-SMA	80	62	72 (3d)
5	10–12	27	34	9	16	Fe-SMA	80	46	75 (3d)
6	13–15	27	34	9	16	Fe-SMA	80	48	47 (1d)
7	16–18	27	34	9	16	Stainless	80	63	74 (3d)
8	19–21	27	34	9	12	Fe-SMA	60	63	74 (3d)
9	22–24	27	34	15	12	Fe-SMA	60	58	77 (3d)
10	25–27	27	34	15	12	Fe-SMA	60	45	77 (3d)

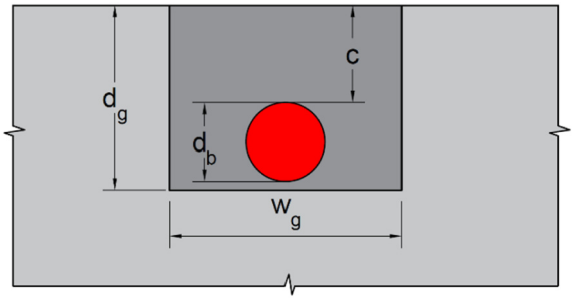

Fig. 4. Geometry of groove.

mean compressive strength f_{cm} of 74.6 MPa after three days of hardening. The development of the tensile strength f_{tm} was similar to that of the compressive strength, as shown in Fig. 3. Mortar compressive strengths between 72 MPa and 77 MPa after three days of hardening were determined.

2.2. Experimental setup

2.2.1. Samples

The test setup consisted of 200 × 200 × 200 mm concrete blocks with eccentrically embedded memory-steel bars. On one surface of the blocks, a groove was cut with two- and three-bladed diamond-saws. The groove depth is indicated with the variable d_g, and the groove width with w_g, as shown in Fig. 4. The cutting process is illustrated in

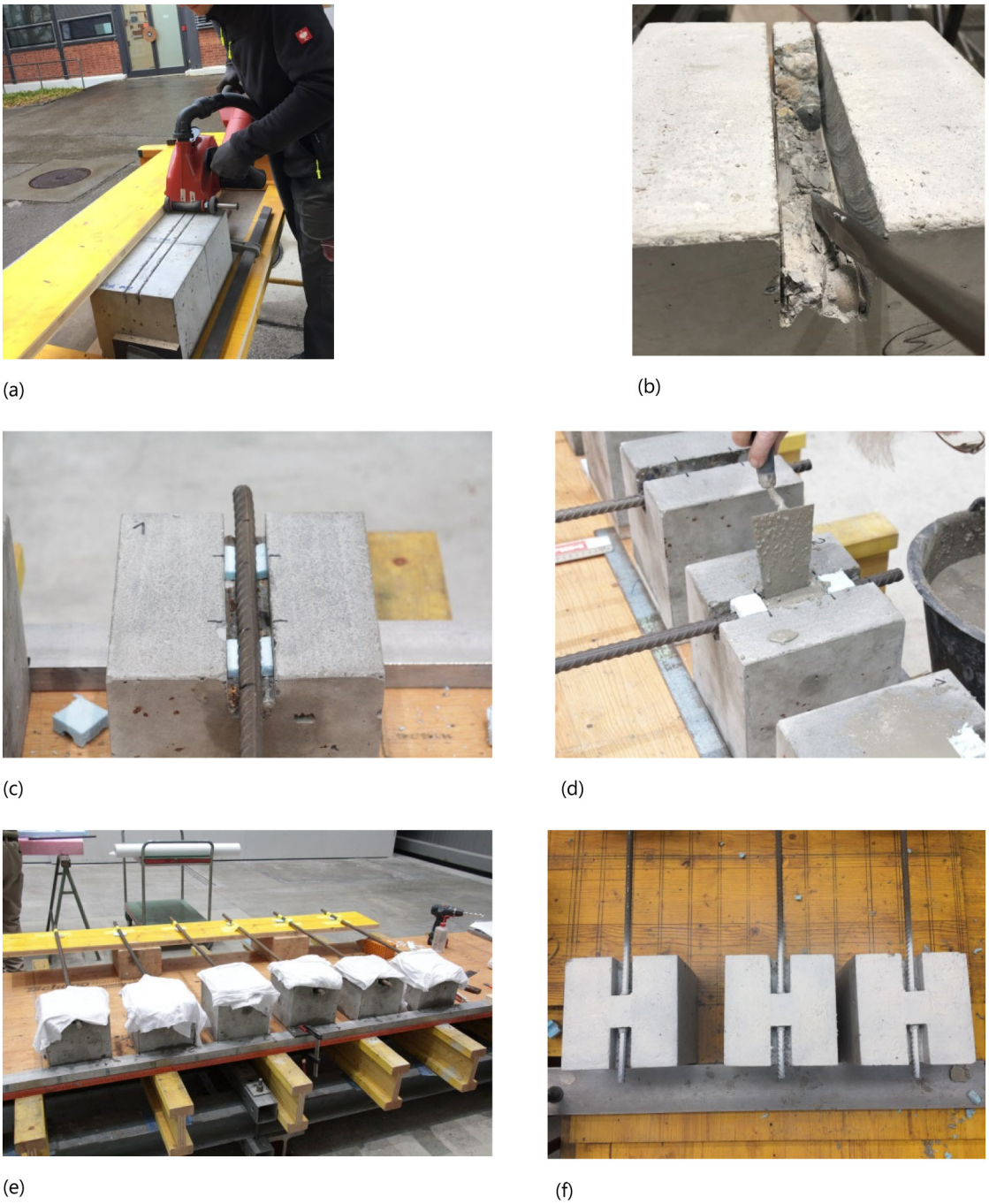

Fig. 5. (a) Cutting of grooves, (b) chiselling of concrete, (c) placement of ribbed bar, (d) casting of mortar, (e) curing of mortar, (f) preparation of specimen for DIC measurement.

Fig. 5(a). After cutting each groove, the remaining concrete substrate between the slits was removed with a chisel, as shown in Fig. 5(b). Different groove geometries were manufactured, as listed in Table 1.

To ensure the best bond properties of the interface between the mortar and concrete, the concrete blocks were submerged in water at least two hours before casting of the mortar in the grooves. Two-piece Styrofoam elements were prepared to hold the memory-steel bars in place and to limit the bond length l_b to five times the bar diameter. Before placing the bars, a thin layer of mortar was poured in the groove. After temporary instalment of the bars (see Fig. 5(c)), the groove was filled with mortar. The casting process is depicted in Fig. 5(d). For Experiments 21–27 (Group 10, see Table 1) with 12 mm bars, no bottom spacer was used for casting to simulate realistic conditions and to maximise the cover size with a limited groove depth. To minimise moisture loss during hardening, the mortar was covered with a wet cloth and plastic foil, as shown in Fig. 5(e). The hardening duration was varied, as shown in Table 1. After the required hardening duration was reached, the surface of the concrete and mortar was sanded to increase the quality of the DIC measurement. The measurement surface was then painted white (see Fig. 5(f)), followed by an irregular black speckle-pattern for image-correlation. The sample geometry is depicted in Fig. 6.

Three different groove geometries were manufactured: the first configuration had a groove depth of 27 mm (~1.5 d_b) and a width of 34 mm (~2.0 d_b). The 27 mm groove depth was chosen to represent a strengthening application for an outside structure with a cover depth of 30 mm. A groove width of 2.0 d_b mm was determined to avoid space problems in the grouting process. The second groove geometry had a depth of 51 mm (~3.0 d_b) and a width of 34 mm (~2.0 d_b) to enable investigation of the effects of groove depth. The third geometry had a groove depth of 27 mm (~1.5 d_b) and a groove width of 51 mm (~3.0 d_b) to enable investigation of the effects of larger groove width. When 12 mm bars were used, the dimensions of 27 × 34 mm were maintained and not adapted to the decreased bar diameter.

2.2.2. Experimental setup and instrumentation

The specimens were placed vertically on the traverse of a servo-hydraulic testing machine of type Amsler with a maximum load capacity of 200 kN. The load was measured with an internal load cell. The concrete block was fixed with a steel beam on the top side to counteract rotation due to torque, induced by the eccentric installation of the bar. The free end of the memory-steel bar was clamped to the testing machine. The machine was programmed to move the traverse upwards in displacement-control at an average rate of 0.008 mm/s. A linear

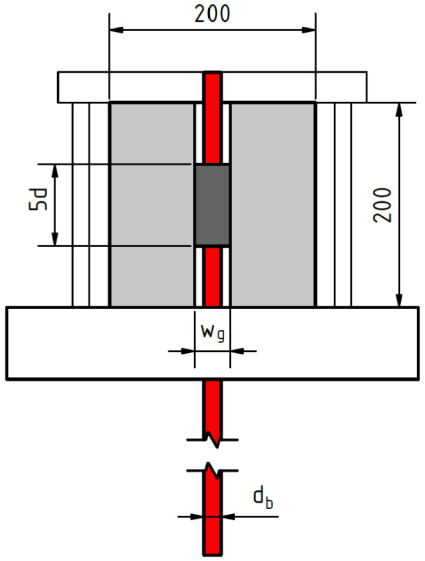

Fig. 6. Drawing of pull-out test sample [mm].

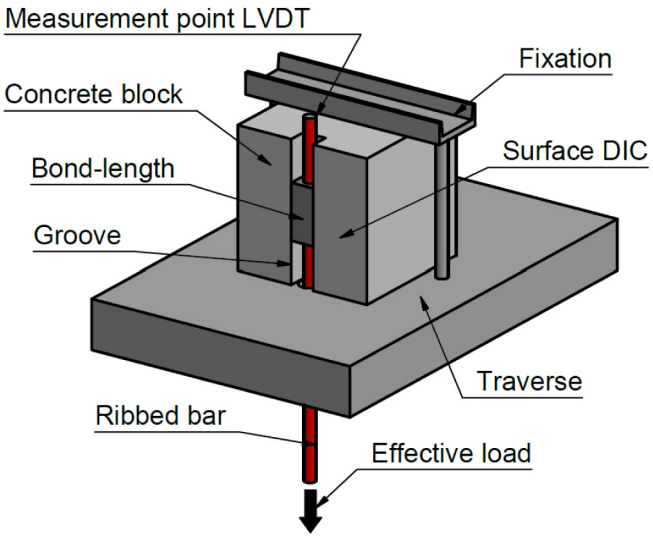

Fig. 7. 3D view pull-out test.

variable differential transformer (LVDT) was installed at the unloaded-end of the memory-steel bar to record the relative displacement between the memory-steel bar and the mortar called free-end slip. A digital image correlation (DIC) system 'ARAMIS' was used to measure the full-field deformation of the concrete, mortar, and bar surfaces, and to obtain the slip of the bar on the loading side. The test setup is illustrated in Figs. 6 to 8. An MGC measurement system by the Swiss company HBM with software Catman was used for recording the measurement.

3. Results and discussion

3.1. Average bond shear stress-slip behaviour

The average bond shear stress τ_b was calculated by dividing the pull-out load F_p by the bonded surface area of the bar (Eq. (1)). As explained in Section 1.4, a constant shear stress distribution is assumed owing to the limited bond length of 5 d_b. The surface area was idealised as a cylinder with nominal bar diameter d_b and length l_b.

$$\tau_b = \frac{F_p}{d_b \, \pi \, l_b} \tag{1}$$

The free-end slip s_{fe} was measured with the LVDT and the DIC system, and the load-side slip s_{ls} was measured only with the DIC system.

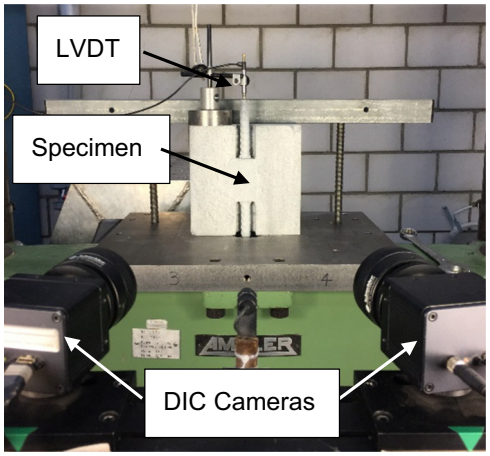

Fig. 8. Front view of pull-out sample with instrumentation.

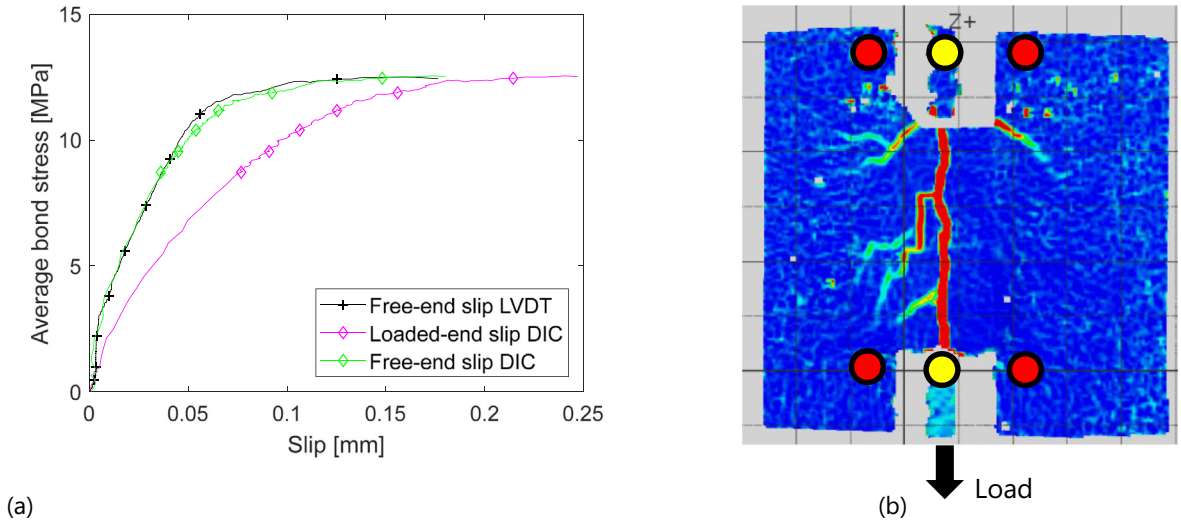

Fig. 9. (a) Comparison of average bond shear stress over loaded-end slip and average bond shear stress over free-end slip from DIC and LVDT measurements, Experiment 3 and (b) principal strains from DIC measurement with measurement points for slip calculation, Experiment 3.

The procedure for calculating the slip consisted of picking three points on the generated deformation surface.

$$s = d_{bar} - \frac{d_{concrete,1} + d_{concrete,2}}{2} \quad (2)$$

Fig. 9(b) displays the principal strain results at peak load, obtained from the DIC measurement of Experiment 3. The red area clearly indicates the longitudinal tensile crack. This figure also shows the position of the picked measurement points for slip measurement. Two points were defined on the solid concrete element (red), whereas one point was defined on the ribbed bar (yellow). The mean value of the concrete displacement was then subtracted from the displacement of the bar to obtain the relative displacement between the bar and the concrete element, which was equal to the slip (see Eq. (2)). This procedure was performed on both the unloaded and loaded sides. Fig. 9 compares the results of both measurement methods and shows the similarity of the results.

In Fig. 10, the maximum average bond shear stress and maximum free-end slips from LVDT measurement at the peak load are shown. For better readability, only mean values for each of the 10 sample groups are indicated. The highest bond shear stress was measured in Group 2 (largest groove depth). The test results are listed in Table 2.

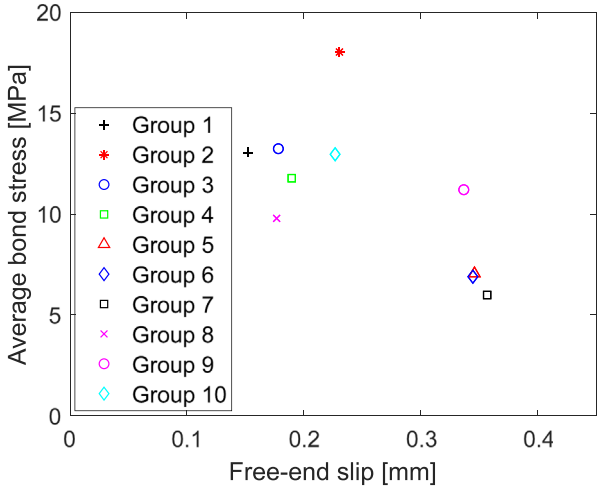

Fig. 10. Average bond shear stresses over free-end slip at peak load.

Fig. 11(a)–(c) indicates the average bond shear stress curves over the free-end slip of all the examined samples. In Groups 1–2 and the first Experiment of Group 4 (Experiment 7), a sudden failure of the bonded connection led to an instant load-drop. The steep decline of the test curve after failure was removed from the graph for better readability. All other test curves depict a softening behaviour with a peak bond shear stress, followed by a gradual decrease, and finally, a section where the slope of the curve approaches zero. The softening branch indicates a gradual damage of the bond between the bar and mortar substrate, followed by residual frictional capacity. The results are summarised in Table 2.

3.2. Failure modes

Based on the crack pattern and presence or absence of a softening branch in the bond shear stress–slip curve, three different failure modes were identified:

3.2.1. Failure mode A: brittle splitting failure

This failure mode is characterized by a sudden failure of the sample with full separation of the bar and mortar cover. As Fig. 11(a) indicates, no softening branch in the bond shear stress–slip behaviour was apparent during this type of failure. Fig. 12(a) illustrates the crack path of a failed sample. At lower load levels, a longitudinal crack started to form in the mortar cover. This type of crack is conventionally attributed to

Table 2
Experimental results, Variables: $\sigma_{max,bar}$ … maximum axial stress in bar, τ_{max} … maximum bond shear stress, $s_{fr,Fmax}$ … free-end slip at peak load, $s_{ls,Fmax}$ … loaded-end slip at peak load, failure modes: A … brittle splitting failure, B … combined splitting and bar pull-out failure, C … failure of concrete block.

Group	$\sigma_{max,bar}$ [MPa]	τ_{max} [MPa]	$s_{fe,Fmax}$ [mm]	$s_{ls,Fmax}$ [mm]	Failure mode
1	261.3	13.1	0.15	0.24	A
2	361.1	18.1	0.23	0.46	C
3	265.0	13.3	0.18	0.27	A
4	235.7	11.8	0.19	0.25	A
5	141.1	7.1	0.35	–	B
6	137.9	6.9	0.39	0.48	B
7	119.7	6.0	0.36	0.38	B
8	204.4	9.8	0.18	0.22	B
9	234.1	11.2	0.34	0.4	B
10	270.8	13.0	0.23	0.29	B

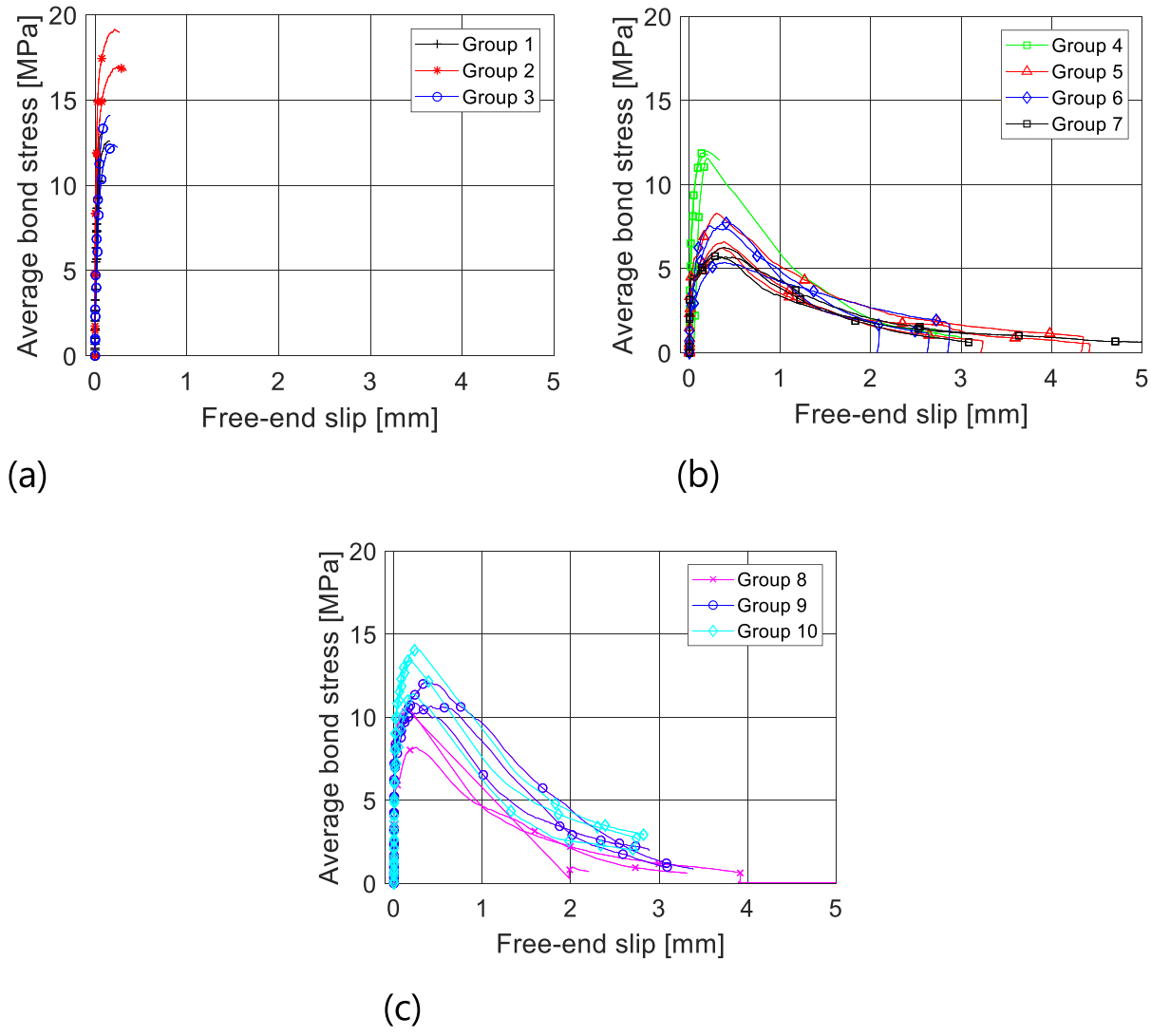

Fig. 11. (a) Average bond shear stress over free-end slip, Groups 1–3: Change in groove geometry, (b) average bond shear stress over free-end slip, Groups 4–7: Change in mortar and concrete strength as well as bar material, (c) average bond shear stress over free-end slip, Groups 8–10: Change in mortar cover, bar diameter.

tangential tensile stresses, caused by radial stresses around the bar [37]. The final failure, however, occurred, when the ultimate tensile capacity of the complete cementitious substrate (groove-filling mortar and concrete) was exceeded. The tensile cracks causing final failure propagated at an angle between 15 and 30° from the horizontal, as indicated in Fig. 12(a). This mechanism is explained further in Section 3.3. When

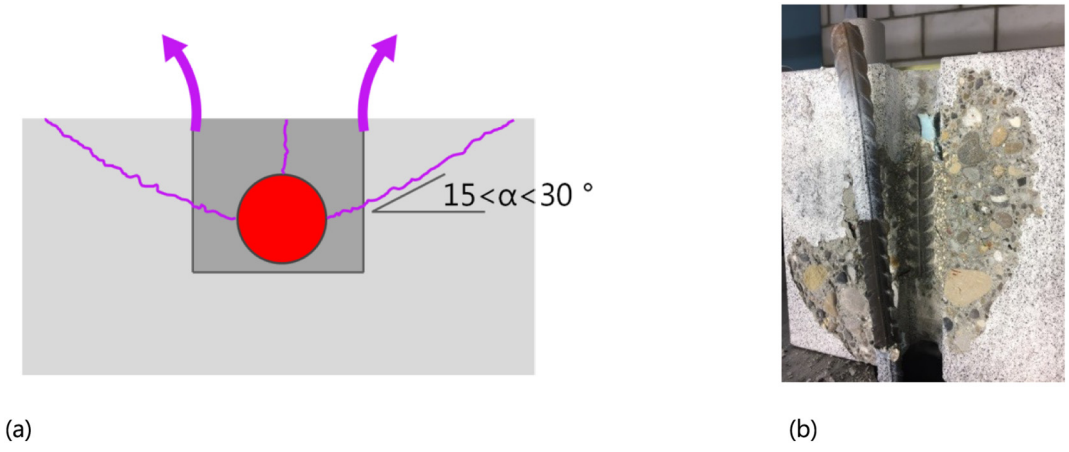

Fig. 12. (a) Illustration failure mode A and (b) example failure mode A.

the failed mortar substrate adjacent to the ribbed bar was examined, no significant signs of shear damage of the mortar substrate were detected. This fact indicates that the mortar strength was sufficient to transfer local compressive stresses. Fig. 12(b) depicts a pull-out specimen after failure.

3.2.2. Failure mode B: combined splitting and bar pull-out failure

In this most common failure mode, a longitudinal splitting crack also occurred in the mortar cover. The final failure however occurred when compressive stresses adjacent to the bar ribs reached levels that led to local compression failure of the mortar corbels, as illustrated in Fig. 13 (a) and (b). Fig. 14 indicates the failure mechanisms based on the position on the bond shear stress–slip curve.

As it is apparent in Fig. 11(a) and (b), this failure mode lead to the appearance of a softening branch in the bond shear stress–slip behaviour, characteristic for bar pull-out failure.

Cracks in the surrounding concrete were also observed in this failure mode, these cracks did not lead to final bond failure as in failure mode A, however. The extent of crack width in the surrounding concrete and mortar varied throughout the experiments.

3.2.3. Failure mode C: failure of concrete block

In one group of samples (Group 2, Experiments 3 and 4), the high capacity of the bonded joint led to a splitting failure of the concrete block, illustrated in Fig. 15(a) and (b), which can be regarded as a secondary failure. Therefore, this experiment does not exhibit the full bond capacity of this configuration but instead indicates a high bond capacity due to large mortar cover.

3.3. Longitudinal cracking of mortar cover

The axial stresses in the bar were mainly transferred through mechanical interaction of the ribs; however, a small part was transferred by adhesion to the surrounding mortar substrate which is usually neglected in the analysis. The compressive stresses adjacent to the ribs were transferred to the material through radial and consequently tangential ring stresses. As a consequence, longitudinal cracking of the mortar cover occurred, starting at low-load levels. Even if the cover was fully cracked with a single longitudinal splitting crack, the load level could increase further, as observed in the experiments. This phenomenon can be explained with the fact that the surrounding substrate is still intact and the final failure occurs due to sudden failure of mortar and surrounding concrete with inclined tensile cracks (failure mode A), or due to local crushing of the mortar adjacent to the bar ribs (failure mode B). In the load-induction zone, a transverse crack developed early due to high local bond shear stress. By means of the DIC-system, the crack width of the longitudinal crack was measured with increasing load. Fig. 16(a) shows the development of the crack width in transverse direction at three different positions along the bond length of

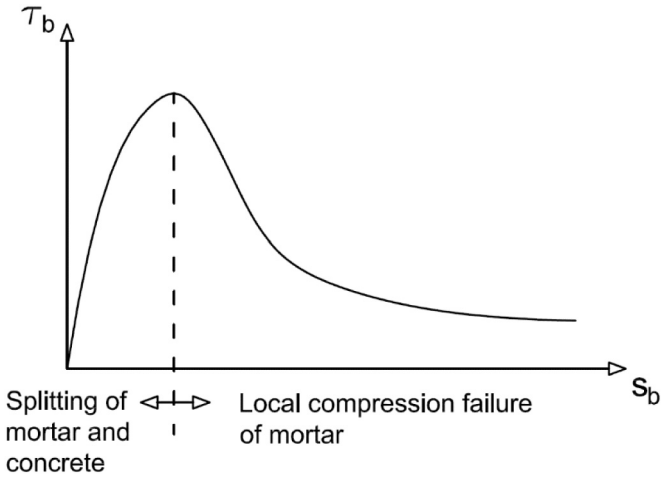

Fig. 14. Illustration of mechanisms, bond shear stress–slip curve.

Experiment 26 (as an example). The position of the measurements is indicated in Fig. 16(b) by letters a–c. It was observed that the crack width on the loaded-end ($w_{c,a}$) increases at a lower load level than on the load-free end ($w_{c,c}$). This behaviour indicates the spread of longitudinal tensile cracks from the load-side towards the free end of the bar.

3.4. Effects of design parameters on bond behaviour

In the following section, the effects of the defined design parameters are explained. In some cases, the maximum bond shear stress was normalised with division by the respective concrete or mortar strength.

3.4.1. Effect of groove geometry

It was observed that specimens with large groove depth, e.g. large mortar cover, had the highest bond shear stresses. The results are listed in Table 3. This effect was largely emphasised by Experiments 3 and 4 (Group 2); however, those samples failed by splitting the whole concrete block, and therefore did not reach the full pull-out capacity. It is assumed that a larger concrete block geometry would lead to higher bond shear stress since the secondary failure mode of block splitting would be avoided. The effect of larger mortar cover arises also by comparing the samples of Group 8 (Experiments 19–21) and 9 (Experiments 22–24). A 19% increase in the average bond shear stress at an increase of the mortar cover by 6 mm was observed. When Experiments 1, 2 (Group 1) and 5, 6 (Group 3) are compared, it is apparent that an increase in the groove width did not have a significant effect on the maximum bond shear stress.

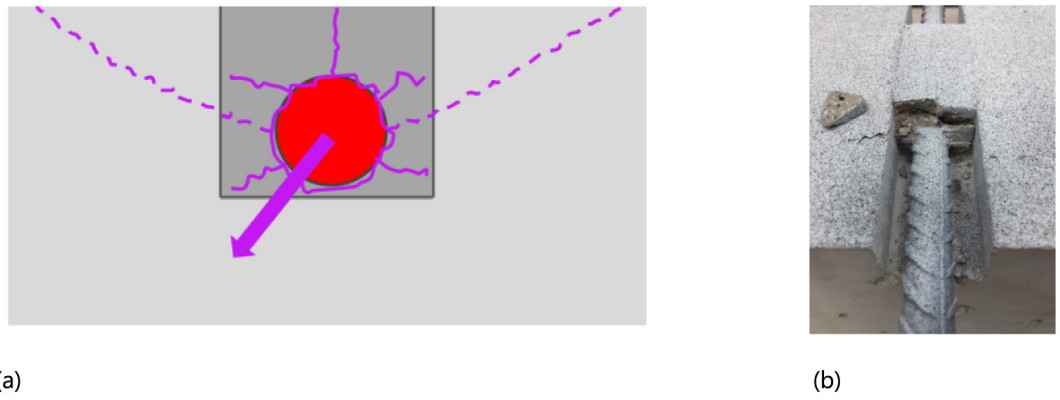

Fig. 13. (a) Illustration failure mode B and (b) example failure mode B.

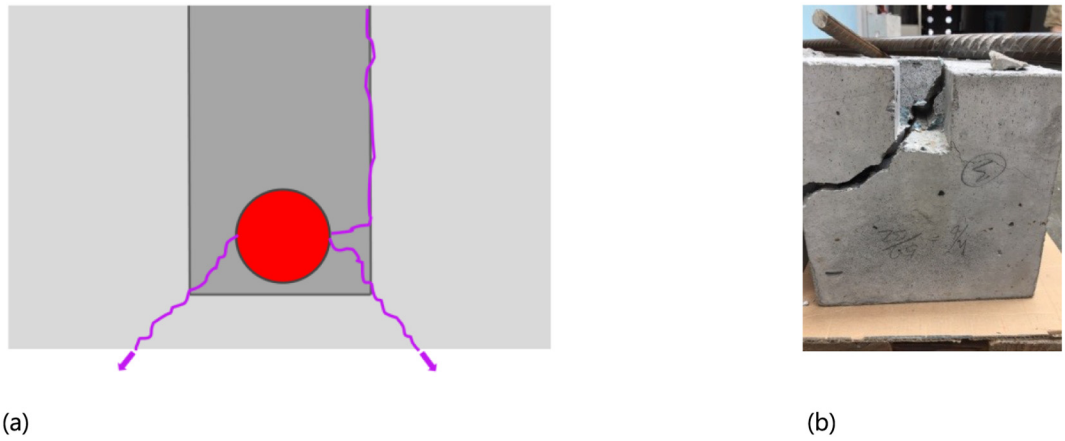

Fig. 15. (a) Illustration failure mode C and (b) example failure mode C.

3.4.2. Effect of concrete strength

When comparing the results (see Table 4) of Groups 4 (Experiments 7–9) and Group 5 (Experiments 10–12), the decrease in concrete strength from 62 MPa to 46 MPa (−35%) resulted in a 42% decrease in average normalised bond shear stress. This result can be explained by the fact that the final failure occurred in the surrounding concrete. The results in this section were normalised by the measured mortar strength.

3.4.3. Effect of mortar strength

The effect of mortar strength is summarised in Table 5. The 23% lower mortar compressive strength of Group 4 led to a 17% decreased maximum normalised bond shear stress of sample Group 1, since the hardening time was decreased from 36 days to 3 days. When Group 1 with a hardening time of 36 days is compared to Group 6 with a hardening time of 1 day, a difference of mortar strength of −50% and a decrease in maximum bond strength of 37% were observed. When comparing sample Groups 4 and 6, the difference between hardening times of 3 days and 1 day leads to a 33% difference in mortar compressive strength and a 32% decrease in normalised maximum bond shear stress. The results indicate that due to the rapid strength development of the mortar, the difference in bond capacity between hardening times of 1 to 3 days was approximately the same as that between 3 and 36 days. The maximum bond shear stress results in this section were normalised by the measured concrete compressive strength.

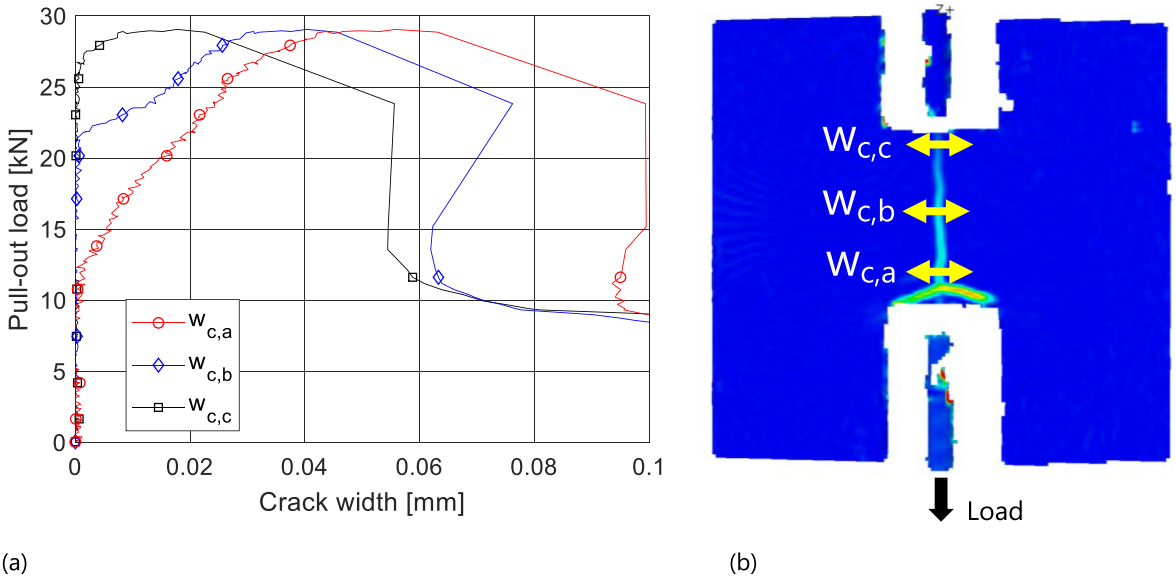

Fig. 16. (a) Pull-out load over crack width w_c of positions a-c of longitudinal tensile crack, Experiment 26, (b) example for DIC measurement of crack width of longitudinal tensile crack, positions a–c, Experiment 26.

Table 3
Effect of cover depth, * … premature failure of sample Group 2 due to splitting of block.

Comparison of Group	Parameter	Change in parameter [mm]	Change in τ_{max} [%]	Failure mode
1 & 2*	Cover depth*	9 to 33*	(+38)*	A to C
8 & 9	Cover depth	9 to 15	+19	B to B
1 & 3	Groove width	34 to 52	+2	A to A

Table 4
Effect of concrete strength.

Comparison of Group	Parameter	Change in parameter [MPa]	Change in τ_{max} [%]	Failure mode
4 & 5	Concrete strength	62 to 46	−42	A to B

Table 6
Effect of bar material.

Comparison of Group	Parameter	Change in parameter [GPa]	Change in τ_{max} [%]	Failure mode
4 & 7	Bar material (elastic modulus)	Memory-steel (122) to stainless steel (200)	−51	A to B

Table 7
Effect of bar diameter.

Comparison of Group	Parameter	Change in parameter [mm]	Change in τ_{max} [%]	Failure mode
4 & 8	Bar diameter	16 to 12	−20	B

3.4.4. Effect of bar material

The effect of the bar material (mainly modulus of elasticity) can be shown by comparing Group 4 (Experiments 7–9) and Group 7 (Experiments 16–18) (see Table 6). Owing to the difference in the stiffness of the ribbed bars of 78 GPa (assuming a mean Young's modulus of 122 GPa for memory-steel in the stress-range of the pull-out experiment), a 51% decrease in maximum normalised bond shear stress was measured. The reason was that with a stiffer bar, a decreased length was needed to transfer a given force, due to decreased strain, which increased the local stresses in the adjacent mortar. The results in this section were normalised by concrete strength and mortar strength.

3.4.5. Effect of bar diameter

The results of Groups 4 (Experiments 7–9) and Group 8 (Experiments 19–21) demonstrate a decrease in maximum normalised bond shear stress by 20% when the bar diameter was reduced at a constant cover depth of 9 mm. The results are listed in Table 7. The experimental results in this section were normalised by concrete strength and mortar strength. In this comparison, it is assumed that the different bond lengths of 60 mm (bar diameter 12 mm) and 80 mm (bar diameter 16 mm) are taken into account by comparison of bond shear stress according to Eq. (1). The increased bond length of Group 4 and the connected increase in pull-out load may still have had an influence on the results; further investigations are therefore suggested. The effect of the bar diameter on the maximum bond shear stress has furthermore been widely investigated in the literature, discussed in [45]. In some cases, it was stated that a decrease in bar diameter leads to larger maximum bond stresses [46,47]. The authors of [48] attributed a great influence of the relative rib area at changing bar diameter to the maximum bond shear stress of pull-out specimens. Other authors [28] did not find significant influence of the bar diameter. In another study [49], these contradictory statements were explained by the change in surface properties when the bar diameter is changed. Therefore, further investigations would clarify the effect of the bar diameter on NSM Fe-SMA bars.

4. Modelling

4.1. Differential equation of bond

As discussed in Section 1.4, the analytical description of a bonded joint can be modelled based on the differential equation of bond behaviour. The basic form of this equation can be modified according to the geometry of the reinforcement type and then solved based on the boundary conditions. The procedure then leads to the specific solutions for bond shear stress, slip, and strain along the longitudinal coordinate *x*. The procedure is explained in this section.

4.1.1. Basic form

Assuming that the concrete base material stiffness is much higher than the bar stiffness ($E_cA_c \rightarrow \infty$), the following formulation based on [45] is obtained for round bars,

$$\frac{d^2 s_b}{dx} - \frac{4}{d_b \cdot E_b} \cdot \tau_b(x) = 0. \tag{3}$$

(For the notations, see Notation list.)

4.1.2. Solution with bilinear bond shear stress–slip law

With respect to later analytical investigations with extended bond length, a bilinear bond shear stress–slip law was selected. If a bilinear bond shear stress–slip relation is assumed and a closed-form solution is required, the differential equation can be solved twice. The equation can be solved first time for the ascending zone (Zone I) and the second time for the descending branch (Zone II) of the bond shear stress-slip law, as was done similarly for externally bonded CFRP strips in [30,50]. These two sections can also be assigned to the bond length, with Zone I describing the undamaged elastic section and Zone II describing the bond damage zone. Fig. 17 illustrates this approach for an example with full bond length, meaning that the bond shear stress decreases to zero at the end of the bond length. The coordinate x_0, where the bond length is separated in the two zones, corresponds to

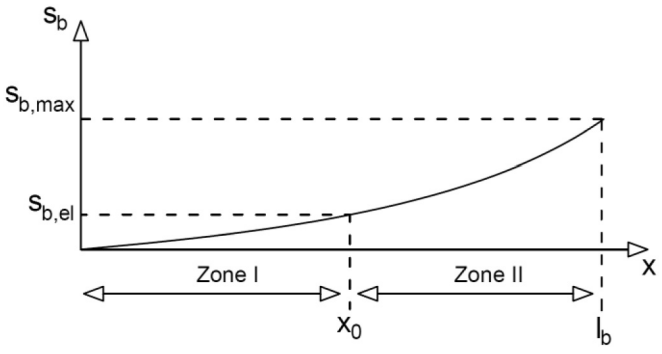

Fig. 17. Illustration of slip distribution over bond length.

Table 5
Effect of mortar strength.

Comparison of Group	Parameter	Change in parameter [MPa]	Change in τ_{max} [%]	Failure mode
1 & 4	Mortar strength (hardening time)	94 to 72	−17	A to A
1 & 6	Mortar strength (hardening time)	94 to 47	−37	A to B
4 & 6	Mortar strength (hardening time)	72 to 47	−32	A to B

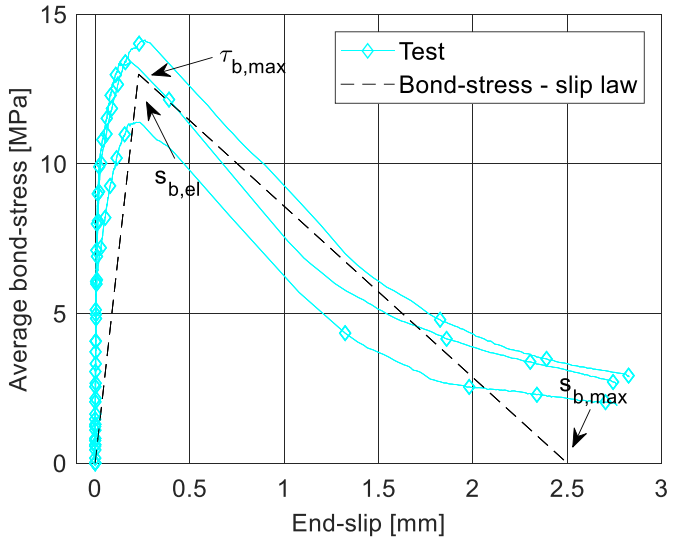

Fig. 18. Example for bilinear bond shear stress-slip law (Group 10).

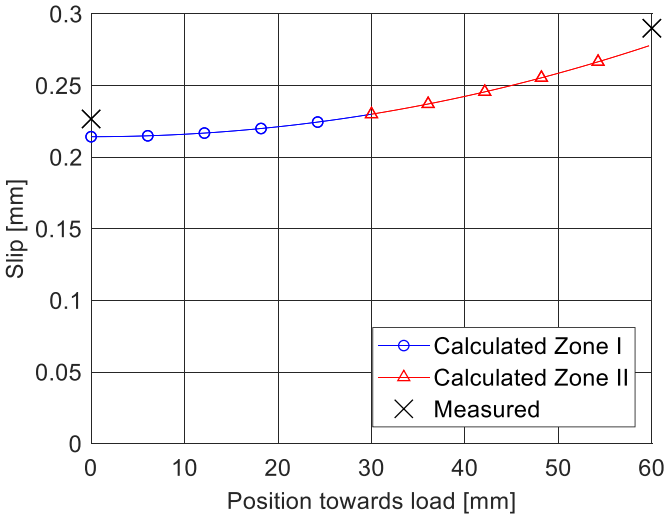

Fig. 20. Calculated slip along bond length and comparison with experimental result, Group 10.

Table 8
Parameters modelling Group 10.

d_b [mm]	l_b [mm]	E_b [GPa]	$\tau_{b,max}$ [MPa]	$s_{b,el}$ [mm]	$s_{b,max}$ [mm]	F_{br} [kN]	$F_{max,test}$ [kN]
12	60	122	13.0	0.23	2.50	27.90	28.13

the point of maximum bond shear stress. A simplified bilinear law was assigned to the experimental results (see Fig. 18). A residual frictional branch was not considered in the analysis. Fig. 18 displays the assigned bond shear stress–slip law in black.

I. Zone I: linear increasing
With the linear increasing bond shear stress–slip relation

$$\tau_b(x) = \frac{\tau_{b,\max}}{s_{b,el}} \cdot s_{bI}(x), \tag{4}$$

the differential equation can be rewritten as

$$\frac{d^2 s_{bI}}{dx} - \frac{4}{d_b \cdot E_b} \cdot \frac{\tau_{b,\max}}{s_{b,el}} \cdot s_{bI}(x) = 0. \tag{5}$$

To enhance readability, the following substitution

$$\omega^2 = \frac{4}{d_b \cdot E_b} \cdot \frac{\tau_{b,\max}}{s_{b,el}} \tag{6}$$

leads to the differential equation of the form

$$\frac{d^2 s_{bI}}{dx} - \omega^2 \cdot s_{bI}(x) = 0. \tag{7}$$

To solve the differential equation, the boundary conditions

$$s_{bI}(x_0) = s_{b,el} \tag{8}$$

$$s'_{bI}(0) = \varepsilon_{bI}(0) = 0 \tag{9}$$

are needed. The specific solution can be obtained as

$$s_{bI}(x) = s_{b,el} \cdot \frac{\cosh(\omega \cdot x)}{\cosh(\omega \cdot x_0)}. \tag{10}$$

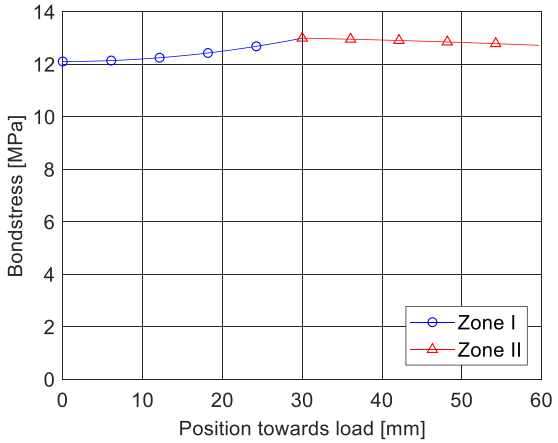

(a)

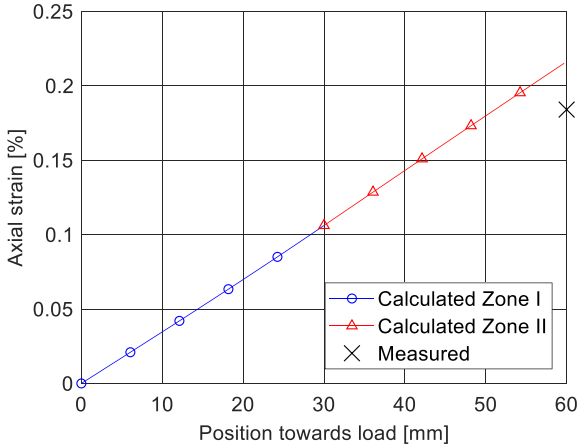

(b)

Fig. 19. (a) Calculated bond shear stress along bond length, Group 10 and (b) calculated axial strain along bond length and comparison with experimental result, Group 10.

Table 9
Parameters modelling Group 4.

d_b [mm]	l_b [mm]	E_b [GPa]	$\tau_{b,max}$ [MPa]	$s_{b,el}$ [mm]	$s_{b,max}$ [mm]	F_{br} [kN]	$F_{max,test}$ [kN]
16	80	122	11.8	0.19	0.40	50.26	47.40

By differentiating once, the strain along the bar can be obtained as

$$\varepsilon_{bI}(x) = s'_{bI} = s_{b,el}\cdot\omega\cdot\frac{\sinh(\omega\cdot x)}{\cosh(\omega\cdot x_0)}. \tag{11}$$

By differentiating a second time and multiplying with $\frac{E_b\cdot d_b}{4}$, the bond shear stress along the bar can be calculated.

$$\tau_b(x) = s''_{bI}\cdot\frac{E_b\cdot d_b}{4} = \omega^2\cdot s_{b,el}\cdot\frac{cosh(\omega\cdot x)}{cosh(\omega\cdot x_0)}\cdot\frac{E_b\cdot d_b}{4} \tag{12}$$

II. Zone II: linear decreasing
With the decreasing bond shear stress–slip relation

$$\tau(x) = \frac{\tau_{b,\,max}}{s_{b,\,max} - s_{b,el}}\cdot\left(s_{b,\,max} - s_{bII}(x)\right), \tag{13}$$

the differential equation can be rewritten as

$$s''_{bII} - \frac{4}{d_b\cdot E_b}\cdot\frac{\tau_{b,\,max}}{s_{b,\,max} - s_{b,el}}\cdot\left(s_{b,\,max}\cdot s_{bII}(x)\right) = 0. \tag{14}$$

For readability reasons, the following substitution

$$\eta^2 = \frac{4}{d_b\cdot E_b}\cdot\frac{\tau_{b,\,max}}{s_{b,\,max} - s_{b,el}} \tag{15}$$

leads to the differential equation of the form

$$s''_{bII} + \eta^2\cdot s_{bII} - \eta^2\cdot s_{b,\,max} = 0 \tag{16}$$

and with the boundary conditions

$$s_{bII}(x_0) = s_{b,el} \tag{17}$$

$$s'_{bII}(x_0) = s'_{bI}(x_0) = \varepsilon_{bI}(x_0) = s_{b,el}\cdot\omega\cdot\tanh(x_0\cdot\omega) \tag{18}$$

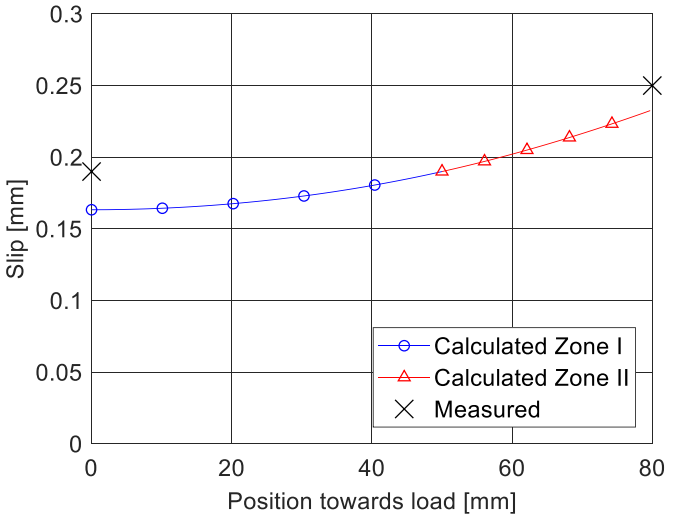

Fig. 22. Calculated slip along bond length and comparison with experimental result, Group 4.

the slip in zone II can be determined:

$$s_{bII}(x) = s_{b,\,max} + \left(s_{b,el} - s_{b,\,max}\right)\cdot\cos(\eta\cdot(x - x_0)) + \frac{\omega\cdot s_{b,el}\cdot\sin(\eta\cdot(x - x_0))\cdot\tanh(\omega\cdot x_0)}{\eta}. \tag{19}$$

By deriving once, the strain in zone II can be calculated:

$$\varepsilon_{bII}(x) = s'_{bII}(x) = -\eta\cdot\left(s_{b,el} - s_{b,\,max}\right)\cdot\sin(\eta\cdot(x - x_0)) + \omega\cdot s_{b,el}\cdot\cos(\eta\cdot(x - x_0))\cdot\tanh(\omega\cdot x_0) \tag{20}$$

and by deriving a second time and multiplying with $\frac{E_b\cdot d_b}{4}$, the bond shear stress can be obtained

$$\tau_b(x) = \left[-\eta\cdot\left(s_{b,el} - s_{b,\,max}\right)\cdot\cos(\eta\cdot(x - x_0)) - \eta\cdot\omega\cdot s_{b,el}\cdot\sin(\eta\cdot(x - x_0))\cdot\tanh(\omega\cdot x_0)\right]\cdot\frac{E_b\cdot d_b}{4}. \tag{21}$$

The maximum load capacity can be determined by using $x = l_b$ in Eq. (20) and Hooke's law:

$$F_{bR} = \varepsilon_{b,\,max}\cdot E_b\cdot\frac{d_b^2\cdot\pi}{4} \tag{22}$$

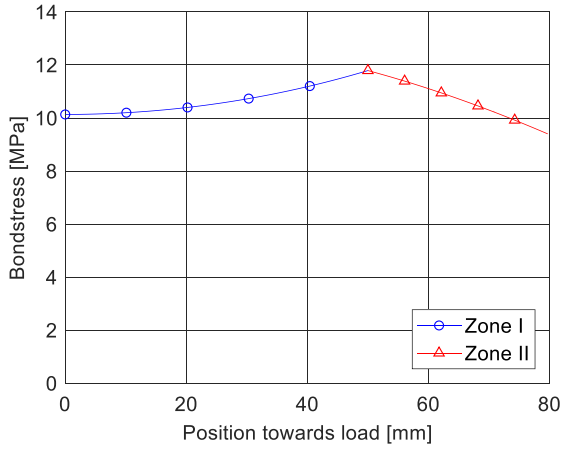

(a)

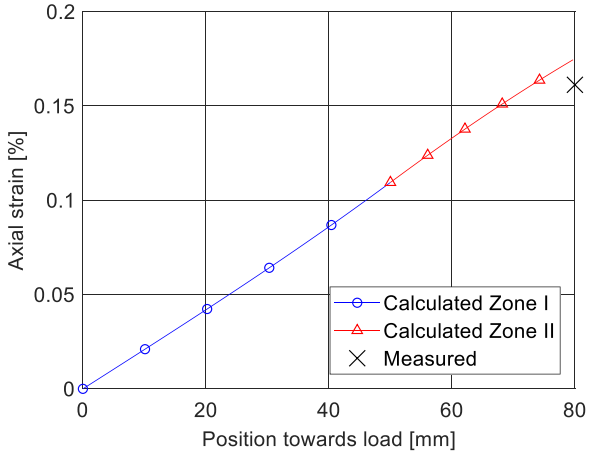

(b)

Fig. 21. (a) Calculated bond shear stress along bond length, Group 4; (b) calculated axial strain along bond length and comparison with experimental result, Group 4.

Table 10
Parameters modelling Group 7.

d_b [mm]	l_b [mm]	E_b [GPa]	$\tau_{b,max}$ [MPa]	$s_{b,el}$ [mm]	$s_{b,max}$ [mm]	F_{br} [kN]	$F_{max,test}$ [kN]
16	80	200	6.0	0.39	2.50	18.19	24.07

4.2. Variable x_0

The variable x_0 describes the location at which the bond length is separated between elastic zone and damage zone. If a bilinear bond shear stress–slip law is assigned, x_0 is also the location of separation between linearly increasing and decreasing bond shear stress–slip law. In [30], x_0 was determined by fitting the measured slip curves. In the next section, the influence of x_0 is discussed in detail.

5. Comparison of experimental results and model

5.1. General

In this section, the analytical model described in Section 4 was used to reproduce current experimental results. The parameters d_b, l_b, and E_b are defined according to the experiments. The parameters $\tau_{b,max}$, $s_{b,el}$, and $s_{b,max}$ were obtained by defining a bilinear BSL according to the experimental bond shear stress–slip curve. The calculated bond capacity F_{br} was then compared to the maximum bond capacity from the respective experiment $F_{max,test}$. The value for x_0 was estimated with a value of 30 mm to take local damage at the load induction zone into account. The influence of different values for x_0 is presented in Section 5.5.

5.2. Modelling of Group 10

In the following section, the configuration with the highest relevance for practical applications (Group 10, Experiments 25–27) was modelled analytically. The maximum load capacity, as well as the slip, strain, and bond shear stress along the bar axis were calculated. The calculated slip was compared with the actual measured values (mean value Experiments 25–27), as listed in Table 8.

For the calculation, a Young's modulus of 122 GPa was used. This value was calculated as the mean value of Young's modulus in the relevant part of the stress-strain curve up to the maximum pull-out load. The value for x_0 was assumed here to be at coordinate x = 30 mm to account for local damages at the load induction zone. The model delivered a maximum load capacity of 27.90 kN. This value fits well into the measured maximum load of 28.13 kN. The maximum slip on the loaded side was calculated as 0.28 mm (Experiment: 0.29 mm). The maximum slip on the load-free end was calculated as 0.21 mm (Experiment: 0.23 mm). Fig. 19(a) shows the calculated bond shear stress over the bonded length. The values indicate an almost constant bond shear stress with a slightly increased stress at the defined point for x_0. The peak bond shear stress at x = 30 mm indicates the transition from Zone I (blue curve) to Zone II (red curve). Fig. 19(b) depicts the calculated axial strain over the bonded length. The curve shows a linearly increasing curve with zero strain at the beginning of the bond length, and the maximum strain at the end. In Fig. 18, the maximum calculated strain is compared to the strain value obtained from the bond experiment. The value was obtained by dividing the maximum load by the nominal cross-section and determining the corresponding strain based on material tests. As represented in Fig. 18(b), the calculated strain at bond coordinate 60 mm shows a similar value as the experimental result.

Fig. 20 displays the calculated slip curve along the bonded length, in addition to the two measured slips. The start of the curve can be

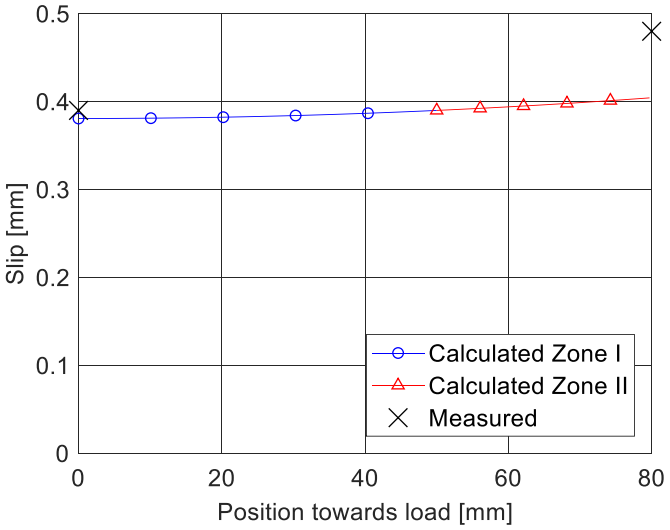

Fig. 24. Calculated slip along bond length and comparison with experimental result, Group 7.

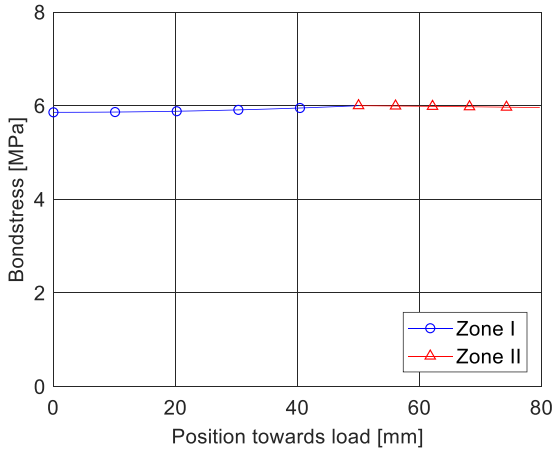

(a)

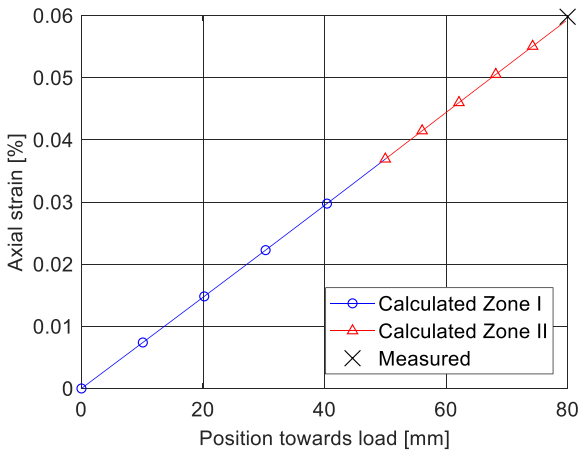

(b)

Fig. 23. (a) Calculated bond shear stress along bond length, Group 7; (b) calculated axial strain along bond length and comparison with experimental result, Group 7.

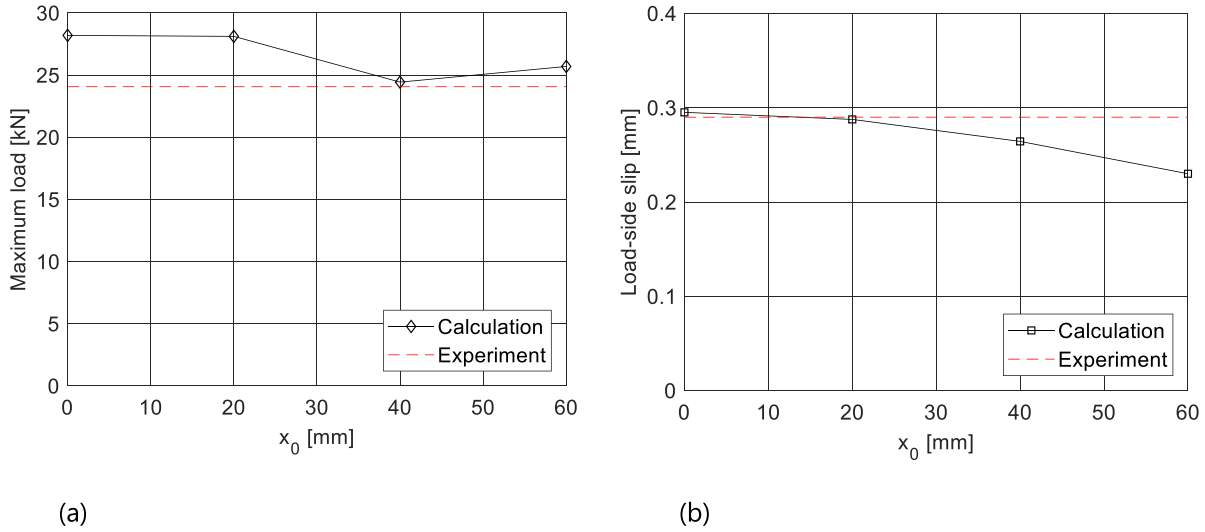

Fig. 25. (a) Influence of x_0 on load capacity (Group 10); (b) influence of x_0 on load-side slip (Group 10).

compared to the measured free-end slip and loaded-end slip. Because a short bond length was used, the end-slip was not zero. This fact was also reproduced in the model, delivering a value similar to that in the experimental results. Correspondingly, the slip on the load-side was reproduced in good accordance.

5.3. Modelling of Group 4

When the bar diameter is increased to 16 mm with an increased bond length of 80 mm and the parameters of the bond shear stress–slip law are modified accordingly, the pull-out capacity increases to 50.26 kN (Experiments 7–9: 47.40 kN), as indicated in Table 9. The value for x_0 here was also set to a distance of 30 mm from the end of the bond length on the load-side, which was equal to an x-coordinate of 50 mm.

Due to the brittle nature of the majority of the samples in this group and the absence of a softening branch in the average bond shear stress–slip test curve, the maximum slip was set to $s_{bmax} = 0.4$ mm. Fig. 21(a) depicts the calculated bond shear stress along the bonded length. At a bond length of 80 mm, the bond shear stress still showed an almost constant behaviour over the bond length. In Fig. 21(b), the calculated axial strain curve is shown, which compares the maximum strain value to the experimental result and demonstrates good agreement between the calculated and measured values.

Fig. 22 shows the calculated slip curve in comparison with the measured values. As indicated in this figure, the calculated values show good accordance with the measurements.

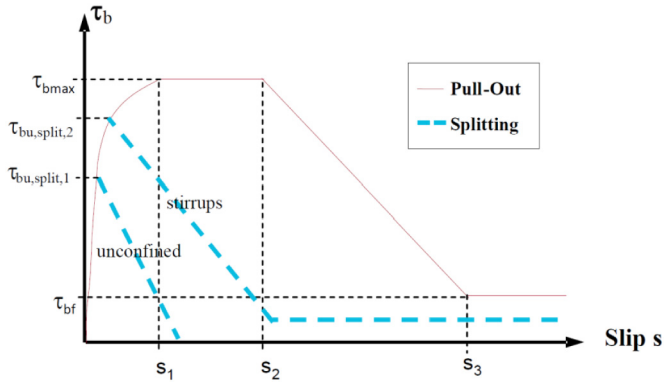

Fig. 26. Analytical bond shear stress–slip relationships, from [51].

5.4. Modelling of Group 7

Group 7 was modelled with a modified Young's modulus of 200 GPa for stainless steel, a bar diameter of 16 mm, a bond length of 80 mm, and the bond shear stress–slip law parameters given in Table 10. The calculated maximum load capacity equalled 18.19 kN (Experiment 24.07 kN).

Fig. 23(a) displays the maximum bond shear stress over the bonded length. Compared to the results of Groups 10 and 4, the curve indicates a lower peak stress, relative to the rest of the curve. In Fig. 23(b), the calculated strain curve is compared to the maximum strain from the bond experiments. The measured strain value was obtained by dividing the maximum load by the nominal bar cross-section and the Young's modulus of 200 GPa. Both values were in good accordance. Fig. 24 illustrates the calculated slip curve over the bonded length. The measured slip values correspond well to the results; however, the ratio between the measured and calculated end-slip was smaller than that of the load-side slip.

To investigate the effects of Young's modulus in the model, the calculation was also performed without modification of the bond shear stress slip law (parameters of Group 4) resulting in a bond capacity of 34.17 kN (compared to 50.26 kN of Group 4). This result indicates the significant effect of Young's modulus in this near-surface-mounted configuration.

5.5. Influence of x_0

To examine the influence of x_0 on the calculated load capacity and load-side slip, the simulation was repeated with the parameters of Section 5.2 (Group 10) and varying values of x_0, as depicted in Fig. 25. As Fig. 25(a) indicates, a decreased value for x_0, which indicates decreased distance to the free end of the bond length, leads to a larger deviation of the calculated load capacity from the experimental values.

Table 11
Estimation of maximum bond shear stress under splitting failure according to fib Model Code 2010 [51].

Group	f_{cm} [MPa]	∅ [mm]	c_{min} [mm]	c_{max} [mm]	$\tau_{bu,split}$ [MPa]	$\tau_{max,test}$ [MPa]
10	48.8	11.5	15	94	12.3	13.0
4	53.6	16	9	92	8.6	11.8
7	55.2	16	9	92	8.7	6.0

Table 12
Parameters for estimation of maximum bond shear stress according to [51] and results.

Group	Curve	Equation	f_{cm} [MPa]	$\tau_{bmax,fib}$ [MPa]	$\tau_{max,Test}$ [MPa]
10	Splitting, stirrups	$\tau_{b\,max} = 8.0 \cdot (\frac{f_{cm}}{25})^{0.25}$	48.8	9.5	13.0
4	Splitting, stirrups	$\tau_{b\,max} = 8.0 \cdot (\frac{f_{cm}}{25})^{0.25}$	53.6	9.7	11.8
7	Splitting	$\tau_{b\,max} = 7.0 \cdot (\frac{f_{cm}}{25})^{0.25}$	55.2	8.53	6.0

However, no clear trend was observed. As Fig. 25(b) shows, a high value for x_0, which means closer to the load-side of the bond length, leads to a high deviation from calculated load-side slip values compared to the experimental values. The comparison also signifies an increasing deviation with increasing value for x_0. Based on these findings, more research is needed to determine the value for x_0.

6. Comparison to existing design recommendation according to fib Model Code 2010

In [51], equations for estimating the maximum bond shear stress of a ribbed bar embedded in concrete were provided. Separate equations for failure mode pull-out and splitting are also provided. Fig. 26 displays the bond shear stress–end-slip curves schematically. It should be noted that the concrete compressive strength is the only parameter that is used to estimate the maximum bond shear stress.

The maximum bond shear stress for splitting was estimated from Eq. (23). The parameter η_2 was taken as 1.0 for good bond conditions, and the term $k_m K_{tr}$ equalled zero due to no confinement reinforcement. The parameters and results are listed in Table 11. The parameter f_{cm} describes the mean cylinder compressive strength, which was estimated as 0.8 times the mean value of concrete and mortar compressive strength. It must be noted that the different Young's moduli of the bars were not considered.

$$\tau_{bu,split} = \eta_2\, 6.5 \left(\frac{f_{cm}}{25}\right)^{0.25} \left(\frac{25}{\varnothing}\right)^{0.2} \left[\left(\frac{c_{min}}{\varnothing}\right)^{0.33} \left(\frac{c_{max}}{\varnothing}\right)^{0.1} + k_m K_{tr}\right] \quad (23)$$

The equations underestimated the bond shear stress of Groups 10 and 4 but overestimated the bond shear stress of Group 7.

Owing to the mixed failure mode of splitting and pull-out, the maximum bond shear stress was also estimated with full bond shear stress according to Fig. 26. For Groups 10 and 4, the curve for splitting failure with stirrups was chosen because of its residual frictional capacity. For Group 7, the curve for unconfined splitting failure was chosen. The parameters and results are listed in Table 12. The results were compared with the experimental values and indicated that the fib procedure always gives lower results than those of the experimental investigation in the case of Groups 10 and 4. However, the fib procedure overestimates the maximum bond shear stress of Group 7.

7. Conclusions

In the current study, the bond behaviour of near-surface-mounted (NSM) ribbed memory-steel bars was investigated. An analytical model was developed based on the differential equation of bond behaviour. The experimental results were compared to the calculated values from the analytical model, as well as existing design recommendations. The following conclusions can be drawn:

- Three main failure modes were identified: A) Brittle splitting failure, B) combined splitting and pull-out failure and C) splitting of the concrete specimen. Failure mode C) occurred due to the limited geometry of the concrete specimen.
- The cover depth decisively influences the bond capacity, with a low cover depth leading to decreased maximum load. The cover depth should therefore be maximised in site applications to avoid premature bond failure.
- The hardening time and hence mortar strength significantly affect the bond strength. A hardening time of 3 days is regarded as an optimum value between duration and load capacity.
- The strength of the surrounding concrete had a significant effect on the bond capacity.
- The lower elastic modulus of memory-steel bars results in a higher bond capacity than if stainless steel bars are used.
- Increasing the groove width does not have a relevant effect on the maximum bond shear stress.
- The behaviour of NSM memory steel-bars can be well represented with a bilinear bond shear stress-slip law. The derived analytical procedure reproduces the load capacity, maximum bar-strain, load-side slip, and end-slip accurately.
- The calculated bond shear stress distributions along the longitudinal coordinate indicates that a constant bond shear stress–slip law may be sufficient for simulating the current results of the experiments with short bond length. However, a bilinear law allows detailed calculation of load-side and free-end slips. Furthermore, the developed bilinear law can also be applied for modelling larger-scale bond tests.
- The value for x_0 was found to influence the obtained bond shear stress, strain and slip curves. Therefore, ongoing studies focus on determining the value for x_0 in more detail.
- Comparison with existing design recommendations indicates considerable deviations in terms of maximum bond shear stress and load capacity.
- The results from this study will be used for future bond research. The developed model can be used to predict the experimental behaviour with full bond length.

Declaration of competing interest

The authors declare that they have no known competing financial interests or personal relationships that could have appeared to influence the work reported in this paper.

Acknowledgements

This study was financed by the Swiss National Science Foundation (SNSF), Grant Number 200021_175998. The support of SNSF is greatly appreciated. The authors would like to thank the technicians of the Structural Engineering Research Laboratory at Empa, Switzerland, for their support in the experiments. Furthermore, gratitude is expressed to the Swiss company re-fer AG for supplying memory-steel reinforcement.

Data availability

The raw/processed data required to reproduce these findings cannot be shared at this time as the data also forms part of an ongoing study.

References

[1] U. Meier, Strengthening of structures using carbon fibre/epoxy composites, Constr. Build. Mater. 9 (6) (1995) 341–351.
[2] C. Escrig, L. Gil, E. Bernat-Maso, Experimental comparison of reinforced concrete beams strengthened against bending with different types of cementitious-matrix composite materials, Constr. Build. Mater. 137 (2017) 317–329.
[3] P. Larrinaga, C. Chastre, H.C. Biscaia, J.T. San-José, Experimental and numerical modeling of basalt textile reinforced mortar behavior under uniaxial tensile stress, Mater. Des. 55 (2014) 66–74.
[4] J. Michels, M. Staśkiewicz, C. Czaderski, R. Kotynia, Y.E. Harmanci, M. Motavalli, Prestressed CFRP strips for concrete bridge girder retrofitting: application and static loading test, J. Bridg. Eng. 21 (5) (2016), 04016003.
[5] M. Motavalli, C. Czaderski, K. Pfyl-Lang, Prestressed CFRP for strengthening of reinforced concrete structures: recent developments at Empa, Switzerland, J. Compos. Constr. 15 (2) (2010) 194–205.
[6] C. Czaderski, M. Shahverdi, R. Brönnimann, C. Leinenbach, M. Motavalli, Feasibility of iron-based shape memory alloy strips for prestressed strengthening of concrete structures, Constr. Build. Mater. 56 (2014) 94–105, https://doi.org/10.1016/j.conbuildmat.2014.01.069.
[7] A. Cladera, B. Weber, C. Leinenbach, C. Czaderski, M. Shahverdi, M. Motavalli, Iron-based shape memory alloys for civil engineering structures: an overview, Constr. Build. Mater. 63 (2014) 281–293, https://doi.org/10.1016/j.conbuildmat.2014.04.032.
[8] P. Soroushian, K. Ostowari, A. Nossoni, H. Chowdhury, Repair and strengthening of concrete structures through application of corrective posttensioning forces with shape memory alloys, Transp. Res. Rec. 1770 (2001) 20–26.
[9] W.J. Lee, B. Weber, G. Feltrin, C. Czaderski, M. Motavalli, C. Leinenbach, Phase transformation behavior under uniaxial deformation of an Fe–Mn–Si–Cr–Ni–VC shape memory alloy, Mater. Sci. Eng. A 581 (2013) 1–7, https://doi.org/10.1016/j.msea.2013.06.002.
[10] W.J. Lee, B. Weber, C. Leinenbach, Recovery stress formation in a restrained Fe–Mn–Si-based shape memory alloy used for prestressing or mechanical joining, Constr. Build. Mater. 95 (2015) 600–610, https://doi.org/10.1016/j.conbuildmat.2015.07.098.
[11] Z. Dong, U.E. Klotz, C. Leinenbach, A. Bergamini, C. Czaderski, M. Motavalli, A novel Fe-Mn-Si shape memory alloy with improved shape recovery properties by VC precipitation, Adv. Eng. Mater. 11 (1–2) (2009) 40–44, https://doi.org/10.1002/adem.200800312.
[12] M. Shahverdi, J. Michels, C. Czaderski, M. Motavalli, Iron-based shape memory alloy strips for strengthening RC members: material behavior and characterization, Constr. Build. Mater. 173 (2018) 586–599, https://doi.org/10.1016/j.conbuildmat.2018.04.057(06/10/2018).
[13] J. Michels, M. Shahverdi, C. Czaderski, R. El-Hacha, Mechanical performance of iron-based shape-memory alloy ribbed bars for concrete prestressing, ACI Mater. J. 115 (6) (2018) 877–886, https://doi.org/10.14359/51710959.
[14] B. Schranz, M. Shahverdi, C. Czaderski, J. Michels, T. Vogel, M. Motavalli, "Ribbed Iron-based Shape Memory Alloy Bars for Pre-stressed Strengthening Applications," Presented at the International Association for Bridge and Structural Engineering Symposium, Guimaraes, Portugal, 27–29th of March, 2019.
[15] J. Michels, M. Shahverdi, C. Czaderski, Flexural strengthening of structural concrete with iron-based shape memory alloy strips, Struct. Concr. 19 (3) (2018) 876–891.
[16] M. Shahverdi, C. Czaderski, M. Motavalli, Iron-based shape memory alloys for prestressed near-surface mounted strengthening of reinforced concrete beams, Constr. Build. Mater. 112 (2016) 28–38, https://doi.org/10.1016/j.conbuildmat.2016.02.174.
[17] S. Abouali, M. Shahverdi, M. Ghassemieh, M. Motavalli, Nonlinear simulation of reinforced concrete beams retrofitted by near-surface mounted iron-based shape memory alloys, Eng. Struct. 187 (2019) 133–148.
[18] M. Shahverdi, C. Czaderski, P. Annen, M. Motavalli, Strengthening of RC beams by iron-based shape memory alloy bars embedded in a shotcrete layer, Eng. Struct. 117 (2016) 263–273, https://doi.org/10.1016/j.engstruct.2016.03.023.
[19] M. Izadi, A. Hosseini, J. Michels, M. Motavalli, E. Ghafoori, Thermally activated iron-based shape memory alloy for strengthening metallic girders, Thin-Walled Struct. 141 (2019) 389–401.
[20] B. Schranz, J. Michels, M. Shahverdi, C. Czaderski, "Strengthening of Concrete Structures With Iron-based Shape Memory Alloy Elements: Case Studies," Presented at the 5th SMAR Conference, Potsdam, Germany, 27–29th of August, 2019.
[21] J. Sena-Cruz, et al., NSM Systems, 19, 2016 303–348, https://doi.org/10.1007/978-94-017-7336-2_8.
[22] H.Y. Lee, W.T. Jung, W. Chung, Flexural strengthening of reinforced concrete beams with pre-stressed near surface mounted CFRP systems, Compos. Struct. 163 (2017) 1–12, https://doi.org/10.1016/j.compstruct.2016.12.044.
[23] H. Rojob, R. El-Hacha, Self-prestressing using Fe-SMA for flexural strengthening of reinforced concrete beams, ACI Struct. J. 114 (2) (2017) https://doi.org/10.14359/51689455.
[24] re-fer AG, re-fer AG website, https://www.re-fer.eu/referenzen/, Accessed date: 20 January 2020.
[25] C. von Bach, Versuche über den Gleitwiderstand einbetonierten Eisens, Mitteilungen Über Forschungsarbeiten Auf Dem Gebiet Des Ingenieurwesens, 22, Springer-Verlag, Berlin 1905, pp. 1–41.
[26] RILEM TC, Bond test for reinforcement steel. 2. Pull-out test, in: RILEM (Ed.), RILEM Recommendations for the Testing and Use of Constructions Materials, E & FN SPON 1994, pp. 218–220.
[27] ASTM C234, Standard test method for comparing concretes on the basis of the bond developed with reinforcing steel, Annual Book of ASTM Standards, 4.02, , 1991.
[28] G. Rehm, Über die Grundlagen des Verbundes zwischen Stahl und Beton, Deutscher Ausschuss für Stahlbeton, Heft 138, Beuth Verlag, Berlin, 1961.
[29] M. Schenkel, Zum Verbundverhalten von Bewehrung bei kleiner Betondeckung, Institute of Structural Engineering (IBK), ETH Zurich, 1998 (PhD).
[30] C. Czaderski, K. Soudki, M. Motavalli, Front and side view image correlation measurements on FRP to concrete pull-off bond tests, J. Compos. Constr. 14 (4) (2010) 451–463.
[31] L. De Lorenzis, A. Rizzo, A. La Tegola, A modified pull-out test for bond of near-surface mounted FRP rods in concrete, Compos. Part B 33 (8) (2002) 589–603, https://doi.org/10.1016/S1359-8368(02)00052-5(2002/12/01).
[32] S.M. Daghash, O.E. Ozbulut, Bond–slip behavior of superelastic shape memory alloys for near-surface-mounted strengthening applications, Smart Mater. Struct. 26 (3) (2017), 035020. https://doi.org/10.1088/1361-665x/26/3/035020.
[33] Fédération Internationale du Béton, Bond and anchorage in fib MC2010, fib Bulletin 72, 2014.
[34] H. Martin, Zusammenhang zwischen Oberflächenbeschaffenheit, Verbund und Sprengwirkung von Bewehrungsstählen unter Kurzzeitbelastung, Deutscher Ausschuss für Stahlbeton (228) (1973).
[35] J. Cairns, K. Jones, The splitting forces generated by bond, Mag. Concr. Res. 47 (171) (1995) 153–165.
[36] R. Eligehausen, H. Kreller, P. Langer, Untersuchungen zum Verbundverhalten gerippter Bewehrungsstäbe mit praxisüblicher Betondeckung, Institut für Werkstoffe im Bauweisen, 1989.
[37] R. Tepfers, Cracking of concrete cover along anchored deformed reinforcing bars, Mag. Concr. Res. 31 (106) (1979) 3–12.
[38] K. Janovic, Verbundverhalten von Bewehrungsstählen unter dauerbelastung in Normal-und Leichtbeton, Deutscher Ausschuss für Stahlbeton (367) (1986).
[39] M. Baldwin, L. Clark, The assessment of reinforcing bars with inadequate anchorage, Mag. Concr. Res. 47 (171) (1995) 95–102.
[40] L. De Lorenzis, J.G. Teng, Near-surface mounted FRP reinforcement: an emerging technique for strengthening structures, Compos. Part B 38 (2) (2007) 119–143, https://doi.org/10.1016/j.compositesb.2006.08.003.
[41] D. Lee, L. Cheng, Bond of NSM systems in concrete strengthening – examining design issues of strength, groove detailing and bond-dependent coefficient, Constr. Build. Mater. 47 (2013) 1512–1522, https://doi.org/10.1016/j.conbuildmat.2013.06.069.
[42] BSI, Stainless steel bars for the reinforcement of and use in concrete — requirements and test methods, British Standards, BS 6744:2001 + A2, 2009, p. 28 , (2009).
[43] Outokumpu Oyj, Tech. Datasheet Stainless Steel Bars Type 1.4162, 2017.
[44] Sika Schweiz AG, Tech. Data Sheet SikaGrout-314, 2017.
[45] M. Auer, Ein Verbundmodell für Stahlbeton unter Berücksichtigung der Betonschädigung, Institute of Concrete Structures and Building Materials, Karlsruhe Institute of Technology, 2015 (75 PhD).
[46] R. Eligehausen, E.P. Popov, V.V. Bertero, Local Bond Stress-Slip Relationships of Deformed Bars Under Generalized Excitations, 1982.
[47] Z.P. Bazant, S. Sener, Size effect in pullout tests, ACI Mater. J. 85 (5) (1988) 347–351.
[48] G. Metelli, G.A. Plizzari, Influence of the relative rib area on bond behaviour, Mag. Concr. Res. 66 (6) (2014) 277–294.
[49] J. Mainz, Modellierung des Verbundtragverhaltens von Betonrippenstahl, Techn. Univ. München, 1993.
[50] T. Ulaga, Betonbauteile mit stab-und lamellenbewehrung: verbund-und zuggliedmodellierung, Institute of Structural Engineering (IBK), ETH Zürich, ETH Zürich, 2003 (PhD).
[51] International Federation for Structural Concrete (fib), fib Model Code for Concrete Structures 2010, 2013 249–250.